ACS Catalysis

Research Article

Cite This: ACS Catal. 2018, 8, 10938−10948

pubs.acs.org/acscatalysis

Rutile Alloys in the Mn−Sb−O System Stabilize Mn^{3+} To Enable Oxygen Evolution in Strong Acid

Lan Zhou,[†] Aniketa Shinde,[†] Joseph H. Montoya,[‡] Arunima Singh,[§,∥] Sheraz Gul,[⊥] Junko Yano,[§,⊥] Yifan Ye,[§,∥,#] Ethan J. Crumlin,[#] Matthias H. Richter,[†,▽] Jason K. Cooper,[§,∥] Helge S. Stein,[†] Joel A. Haber,[†] Kristin A. Persson,*[,‡,§,○] and John M. Gregoire*[,†]

[†]Joint Center for Artificial Photosynthesis, California Institute of Technology, Pasadena, California 91125, United States

[‡]Environmental Energy Technologies Division, Lawrence Berkeley National Laboratory, Berkeley, California 94720, United States

[§]Joint Center for Artificial Photosynthesis, Lawrence Berkeley National Laboratory, Berkeley, California 94720, United States

[∥]Chemical Sciences Division, Lawrence Berkeley National Laboratory, Berkeley, California 94720, United States

[⊥]Molecular Biophysics and Integrated Bioimaging Division, Lawrence Berkeley National Laboratory, Berkeley, California 94720, United States

[#]Advanced Light Source, Lawrence Berkeley National Laboratory, One Cyclotron Road, Berkeley, California 94720, United States

[▽]Division of Chemistry and Chemical Engineering, California Institute of Technology, Pasadena, California 91125, United States

[○]Department of Materials Science and Engineering, University of California, Berkeley, California 94720, United States

Supporting Information

ABSTRACT: Electrocatalysis of the oxygen evolution reaction is central to several energy technologies including electrolyzers, solar fuel generators, and air-breathing batteries. Strong acid electrolytes are desirable for many implementations of these technologies, although the deployment of such device designs is often hampered by the lack of non-precious-metal oxygen evolution electrocatalysts, with Ir-based oxides comprising the only known catalysts that exhibit stable activity at low overpotential. During our exploration of the Mn−Sb−O system for precious-metal-free electrocatalysts, we discovered that Mn can be incorporated into the rutile oxide structure at much higher concentrations than previously known, and that these Mn-rich rutile alloys exhibit great catalytic activity with current densities exceeding 50 mA cm^{-2} at 0.58 V overpotential and catalysis onset at 0.3 V overpotential. While this activity does not surpass that of IrO_2, Pourbaix analysis reveals that the Mn−Sb rutile oxide alloys have the same or better thermodynamic stability under operational conditions. By combining combinatorial composition, structure, and activity mapping with synchrotron X-ray absorption measurements and first-principles materials chemistry calculations, we provide a comprehensive understanding of these oxide alloys and identify the critical role of Sb in stabilizing the trivalent Mn octahedra that have been shown to be effective oxygen evolution reaction (OER) catalysts.

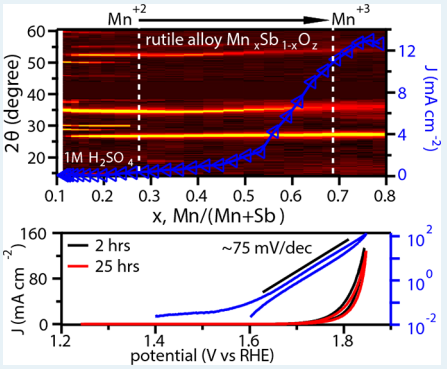

KEYWORDS: *oxygen evolution reaction, catalysis, electrochemical stability, metal oxide alloys, combinatorial materials science*

1. INTRODUCTION

The development of active, stable, and earth-abundant oxygen evolution catalysts in acid environments has drawn great interest in materials chemistry research and for technological applications such as metal winning and renewable solar fuel synthesis.[1] Solar fuel generators that use renewable energy to photoelectrochemically synthesize fuel couple the oxygen evolution reaction (OER) to a fuel-forming reaction, typically hydrogen evolution or carbon dioxide reduction. The OER half reaction requires 4 coupled electron and proton transfers, resulting in sluggish kinetics and consequently a large overpotential; therefore, a highly active catalyst is important to maximize the energy conversion efficiency.[2] While cost-effective, earth-abundant, efficient, and robust OER catalysts have been found for alkaline or neutral media applications,[3] modeling and experimental demonstrations have shown that an acidic environment is more desirable for high-efficiency fuel-forming devices.[4] The only established acid-stable OER catalysts are based on noble-metal oxides such as IrO_x and RuO_x that simultaneously exhibit high catalytic activity and stability in the corrosive acid environment.[1]

Received: July 10, 2018
Revised: October 5, 2018
Published: October 16, 2018

DOI: 10.1021/acscatal.8b02689
ACS Catal. 2018, 8, 10938−10948

Discovering and developing acid-stable, earth-abundant OER catalysts that achieve useful rates of oxygen evolution has proven to be very challenging, especially for low-overpotential operation. Significant materials research efforts to meet this challenge include: (1) mixing noble metals (Ir, Ru) with non-noble metals (W,[5] Sn,[6] Sn−Sb,[7] Sn−Nb,[8] Mn,[9] Ti,[10] Ta,[11] Ni,[12] Co[13]) to achieve acid-stable, high activity with minimal noble-metal content; (2) exploring noble-metal-free transition-metal oxides (Co-based,[14] Fe-based,[15] and Mn-based[16]); and (3) designing high-order multication metal oxides combining the activity of one or more metal oxides with the acid stability of other metal oxides to produce a new earth-abundant material displaying active, acid-stable OER catalysis.[16]

MnO_x-based catalysts are among the most studied non-noble-metal OER catalysts due to inspiration from the $CaMn_4O$ cluster in the photosynthetic oxygen evolution center (OEC) and efficacy of Mn-based catalysts across a broad range of reactions, which is related to the large number of accessible oxidation states and the ensuing diverse oxide stoichiometries and polymorphs of MnO_x.[17] The presence of Mn^{3+} in heterogeneous catalysts is correlated with OER activity, which has limited the activity of MnO_x-based OER catalysts in neutral to acidic conditions as Mn^{3+} disproportionates to Mn^{2+} and Mn^{4+} at pH < 9.[18] The recognition of the critical role played by Mn^{3+} in OER catalysis has led to efforts to stabilize this oxidation state in neutral and acidic pH electrolytes.[19] Of particular note for OER under acidic conditions are the stability and moderate activity of electrochemically activated manganese oxide; under specific deposition conditions, a cathodically treated or cyclic-voltammetry-deposited (CV-deposited) MnO_x film is proficient for the OER due to generation of Mn^{3+} on the surface of the $Mn^{4+}O_2$ electrode.[20] This catalyst preparation proceeds by the *in situ* comproportionation of Mn^{4+} with Mn^{2+} to produce metastable, OER-active Mn^{3+} ions trapped in tetrahedral coordination sites within the MnO_2 matrix, which are protected from both dissolution and disproportionation under OER conditions.[21] At relatively low overpotentials producing relatively low current densities of 0.1 mA cm^{-2}, this electrochemically activated manganese oxide exhibits stable operation in acid (pH 0.3−3), but application of higher overpotentials to increase the current density leads to manganese oxidation and film dissolution as permanganates,[20c] motivating exploration of materials strategies for stabilizing MnO_x at OER potentials in strong acid, which is the focus of the present work.

Among these materials-based approaches to Mn stabilization is our previous exploration of stabilizing Co and Mn active sites with multication oxides in the $(Co−Mn−Ta−Sb)O_x$ system, which includes the compositions presented in this work but without control or characterization of the crystal structure, which we show here to be critical to both activity and stability.[16a] Huynh, M et al. reported that $CoMnO_x$[16b] (where XPS shows Mn is Mn^{4+}, which is relatively inactive for OER) could be operated stably at low overpotential and current density and suffered from corrosion due to the insufficient stability of both Co and Mn cations. Patel et al. reported cubic structure of F-doped $Cu_{1.5}Mn_{1.5}O_4$ nanoparticles containing both Mn^{3+} and Mn^{4+}, where the high catalytic activity was attributed to the high oxidation potential of the F anions.[16c] Recently, crystalline nickel−manganese antimonates with a rutile-type structure were reported in 1.0 M H_2SO_4 with overpotential at 10 mA cm^{-2} increasing from 672 ± 9 to 735 ± 10 mV over 168 h of continuous operation.[16d,22] In the present work, we return the focus to the Mn−Sb pseudobinary system using combinatorial methods, which have been previously deployed for exploring OER catalysts in acid,[23] to explore the relationship between physical properties and OER electrocatalytic activities of sputter-deposited composition-spread thin films. We combine combinatorial synthesis and electrochemistry with a range of structural, spectroscopic, and computational characterization to discover Mn-rich rutile alloys of the type $(Mn_xSb_{1-x})O_2$ with $x > 0.5$, quantify the stabilization of Mn provided by the Sb-based rutile oxide structure, and reveal alloying-based tuning of the Mn oxidation state and the covalency of Mn−O bonds that leads to high OER activity at Mn-rich compositions.

2. EXPERIMENTAL SECTION

2.1. Physical Vapor Deposition (PVD) Library Synthesis. The Mn−Sb binary oxide composition libraries $Mn_xSb_{1-x}O_z$ were fabricated using reactive radio frequency magnetron cosputtering of Mn and Sb metal targets onto 100 mm diameter Pt/Ti/SiO_2/Si substrates in a sputter deposition system[24] (Kurt J. Lesker, CMS24) with 10^{-5} Pa base pressure. The thermally grown SiO_2 served as a diffusion barrier, the Ti as an adhesion layer, and the Pt as a common back contact for the composition library. The Mn−Sb oxide thin films were deposited under 0.80 Pa working atmosphere composed of inert sputtering gas Ar (0.72 Pa) and reactive gas O_2 (0.08 Pa). The composition gradients in the cosputtered continuous composition spreads were attained by positioning the deposition sources in a nonconfocal geometry. The deposition proceeded for 1 h with the power on the Sb and Mn source at 24 and 146 W, respectively. The as-deposited composition library was cut into 3 pieces with similar composition gradient; the center strip was subsequently placed flat on a quartz support and annealed in air in a programmable Thermo Scientific box oven at 700 °C for 3 h. The annealing was preceded by a 2 h temperature ramp and was followed by natural cooling. The bottom strip was annealed similarly at 550 °C for 10 h. A second deposition proceeded with a higher O_2 partial pressure of 0.16 Pa (total pressure of 0.8 Pa kept the same) in the sputter gas to provide a higher oxygen concentration in the as-deposited film since no postdeposition thermal processing was applied to this composition library.

2.2. OER Catalytic Measurements. The OER performance of the $Mn_xSb_{1-x}O_z$ catalysts was evaluated using a previously reported scanning droplet cell (SDC)[25] with flowing O_2-saturated 1.0 M H_2SO_4(aq) electrolyte solution (pH = 0.13). The 3-electrode cell includes a Pt counter electrode, Ag/AgCl reference electrode, Gamry G 300 potentiostat, and custom LabVIEW software. The SDC moved along the binary composition library and performed an experiment every 3 mm. The activity of each $Mn_xSb_{1-x}O_z$ composition was characterized using cyclic voltammetry (CV) measurements from 1.24 to 1.79 V and back to 1.24 V versus reversible hydrogen electrode (RHE) at a scan rate of 0.02 V s^{-1}. A droplet contact area of approximately 0.02 cm^2 was assumed for calculation of current density. Chronoamperometry (CA) measurements at an applied potential of 1.69 V vs RHE for 200 s were used to test OER stability of films with Mn compositions $x \geq 0.33$.

Further electrochemical characterization of epoxy-encapsulated $Mn_xSb_{1-x}O_z$ electrodes was conducted after SDC measurements. An electrochemical H-cell was filled with 175 mL of O_2-saturated 1.0 M H_2SO_4 electrolyte (pH 0); a

DOI: 10.1021/acscatal.8b02689
ACS Catal. 2018, 8, 10938−10948

standard calomel reference electrode and carbon rod counter electrode were separated by a fine-porosity glass frit. A magnetic stir bar and O_2 bubbling provided constant electrolyte mixing. Measurements were conducted with a Gamry 600 potentiostat and Gamry Framework software. The uncompensated resistance of the cell was determined by electrochemical impedance spectroscopy (EIS) in static 1.0 M H_2SO_4 electrolyte at 1.72 V vs RHE in the frequency range from 1 Hz to 300 kHz.

2.3. Theoretical Calculations. To investigate the various possible structures corresponding to the synthesized Mn−Sb oxide catalysts, density functional theory (DFT) calculations were conducted on a set of intermetallic oxide phases in the Mn−Sb−O chemical system mined from the Materials Project (MP) database.[26] In addition, these structures were supplemented with compositional perturbations of each structure that were generated by combinatorial substitution of 1−2 Mn for Sb and *vice versa*. Lastly, two non-Mn containing compounds, rutile TiO_2 and a trirutile phase of $CoSb_2O_6$ (mp-24845), were used as templates for an additional set of structures. In the case of TiO_2 compositional perturbations of a 2 × 2 × 2 $MnSbO_4$ supercell were determined. In the case of $CoSb_2O_6$, elemental substitutions that spanned every ordered approximation of a disordered structure of intermetallic oxide phases at compositions of $Co_xSb_{1-x}O_2$ were determined for x = 0, 1/6, 1/3, 1/2, 2/3, 5/6, and 1. Relaxation of these structures was performed using automated Vienna *ab initio* simulation package (VASP) DFT routines,[27] resulting in MP-compatible total energies and electron densities. Data corresponding to the results of these calculations are available on www.materialsproject.org. Calculated energies were used to construct compositional phase diagrams in Mn−Sb−O space, grand potential phase diagrams with a fixed chemical potential of oxygen reflecting stable Mn−Sb oxides under synthesis conditions, and Pourbaix diagrams to determine the electrochemical phase stability under OER potentials at acidic pH. Each of these analyses uses pymatgen's phase and Pourbaix diagram[28] tools directly, and analysis code is available by request. Lastly, Bader charge calculations[29] were conducted on the calculated charge densities to determine oxidation-state trends between compositions. Additional details about the optimized structures, templates, and calculation parameters are provided in the SI.

2.4. Materials Characterization. The crystal structures and phase distribution of $Mn_xSb_{1-x}O_z$ binary composition libraries were determined by the powder X-ray diffraction (XRD) technique using a Bruker DISCOVER D8 diffractometer with Cu Kα radiation from a Bruker IμS source. The X-ray spot size was limited to a 1 mm length scale, over which the composition is constant to within approximately 1%. The XRD measurements were performed on a series of evenly spaced positions along the composition gradient. Diffraction images were collected using a two-dimensional VÅNTEC-500 detector and integrated into one-dimensional patterns using DIFFRAC.SUITE EVA software.

To determine the library composition, X-ray fluorescence (XRF) measurements were performed on an EDAX Orbis Micro-XRF system with an X-ray beam approximately 2 mm in diameter. Since the XRF sampling depth far exceeds the film thickness, XRF counts for each element were assumed to be proportional to the number of corresponding atoms present in the film, and the sensitivity factor for each element was calibrated using commercial XRF calibration standards (Micromatter). These measurements provide evaluation of elemental loss with better than 1% sensitivity.

X-ray photoelectron spectroscopy (XPS) survey spectra were measured to determine the near-surface chemistry for using a Kratos Axis Ultra instrument with excitation from a monochromatized Al Kα radiation at 150 W (10 mA at 15 kV). The collected spectra were calibrated to the carbon 1s peak of 284.8 eV.

Ambient pressure XPS (AP-XPS) measurements were performed at Beamline 9.3.2 of the Advanced Light Source, Lawrence Berkeley National Laboratory.[30] H_2O adsorption on samples $Mn_{0.70}Sb_{0.30}O_z$ and Mn_2O_3 were performed by dosing 0.2 Torr H_2O at 298 K; meanwhile the surface chemistry was investigated by performing the AP-XPS measurements. The low-resolution survey with a binding energy from 700 to −5 eV was collected at an incident photon energy of 770 eV. The high-resolution Sb 3d and O 1s, and Mn 2p, XPS spectra were collected at an incident photon energy of 670 and 770 eV, respectively. For each condition, samples were equilibrated for at least 90 min before the measurement. By taking spectra at different sample spots and comparing spectra before and after beam illumination for 2 h, we found beam damage on the sample is negligible during the measurements.

X-ray absorption spectroscopy (XAS) is an element specific spectroscopic technique and is very sensitive to oxidation states. The Mn and Sb K-edge XAS measurements were carried out on Beamline 7-3 at the Stanford synchrotron radiation light source (SSRL) along with the standard references Sb^{5+} (Sb_2O_5), Mn^{2+} (MnO), Mn^{3+} (Mn_2O_3), Mn^{4+} (MnO_2), and mixed Mn^{2+}/Mn^{3+} (Mn_3O_4). The quantitative analysis of XAS data was carried out by linear combination fitting (LCF) using a database of pure-valence species (the Combo method) as reported by Manceau et al.[31] Further details are reported in the SI.

Inductively coupled plasma mass spectrometry (ICP-MS) was used to determine the concentration of dissolved metals in electrolyte used for electrochemistry at different durations over the course of CV cycling. ICP-MS data were collected using an Agilent 7900 ICP-MS instrument. The composition and loading of the $Mn_xSb_{1-x}O_z$ electrode deposited on fluorine-doped tin oxide (FTO) was obtained by electrochemically dissolving the film in 27 mL of 20% HNO_3 and cycling the potential with respect to a carbon rod. The samples were diluted to approximately 2% HNO_3 in milli-Q water. Standard and blanks were prepared in trace metals grade 2% HNO_3 diluted in milli-Q water. The standard curve included concentrations 0.1, 1.0, 10.0, 100, 500, and 1000 ppb and was linear over this range. All sample concentrations fell within the concentration range described by the calibration curves. The internal standard (Agilent 5188-6525) was used.

3. RESULTS AND DISCUSSION

3.1. Catalyst Discovery via Combinatorial Electrochemistry. The OER catalytic activity of $Mn_xSb_{1-x}O_z$ composition library was assessed in 1.0 M H_2SO_4 (pH 0.13) aqueous solution using libraries deposited at 3 different temperatures onto Si substrates with a Pt conducting layer. Figure S4 shows the series of CVs obtained from the binary composition library annealed at 700 °C when the applied potential was scanned at 0.02 V s^{-1} in the range 1.24−1.79 V vs RHE. The same CV was performed on a series of compositions from the library annealed at 550 °C, and 3 cycles of this CV were applied to a series of compositions from

DOI: 10.1021/acscatal.8b02689
ACS Catal. 2018, 8, 10938−10948

the library that was not annealed after deposition. XRD characterization was performed on each library, and the maximum current from the CVs is plotted with the XRD heat map in Figure 1.

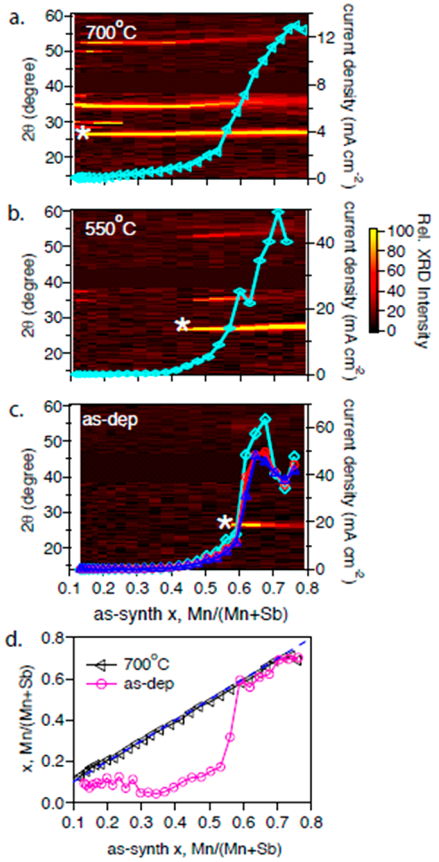

Figure 1. (a–c) Two-dimensional XRD plots of 3 $Mn_xSb_{1-x}O_z$ libraries annealed at 700 °C, at 550 °C, and as-deposited. In each heat map image, each data column corresponds to a 1D XRD pattern at that composition, and the most Sb-rich observation of the rutile [110] peak is indicated with a white * that moves to higher Mn concentration with decreasing temperature. The current densities obtained at 1.79 V vs RHE in CV measurements on 3 libraries in 1.0 M H_2SO_4 aqueous solution are superimposed on the corresponding XRD maps. For the as-deposited library, 3 consecutive CVs were performed, and their maximum current density values are plotted in the order of cyan, red, and blue. (d) XRF-determined composition change after CV measurements for libraries annealed at 700 °C (1 CV cycle) and without annealing (3 CV cycles).

Across the 3 types of processing, the maximum current density not only increases with decreasing annealing temperature but also becomes more sensitive to film composition due to the tighter window of rutile alloy formation. The sharp increase in current density at the onset of rutile crystallization in the as-deposited library is quite striking. Figure 1d also illustrates that, for a given composition, Mn corrosion is lower when the film crystallizes into the rutile structure, demonstrating that this structure improves both activity and stability, as further discussed below. When the film crystallizes into the rutile structure at the same composition, higher activity is observed with lower annealing temperature, which may be due to increased nanocrystallinity, which is a common strategy for creating active catalyst sites.[1b] While these results indicate opportunities for catalyst optimization via nanostructuring, continued evaluation of the rutile oxide catalysts in the present work proceeds with annealed films as they are more amenable to the characterization required to elucidate the underpinnings of the improved activity and stability.

To continue assessment of the initial stability, a subset of samples from the 700 °C library were measured at 1.69 V vs RHE (460 mV overpotential) for 200 s. The CA data are shown in Figure S7, and the current at the end of each measurement is shown in Figure 2a, revealing an increase in current density with increasing Mn concentration for the 4 phase-pure rutile samples, followed by a slight decrease at x = 0.72 where some Mn_2O_3 is present in the as-synthesized film, confirming that Mn-rich rutile oxide alloys provide the highest catalytic activity.

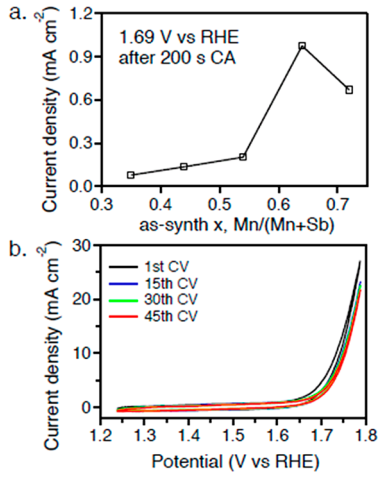

Figure 2. (a) Current density after 200 s CA measurement at 1.69 V vs RHE in 1.0 M H_2SO_4 aqueous solution (CA data are shown in Figure S7). (b) Current density vs potential for $Mn_{0.67}Sb_{0.33}O_z$ film deposited on FTO and annealed at 550 °C in 1.0 M H_2SO_4 solution initially (1st CV) and after 15, 30, and 45 CV sweeps between 1.24 and 1.79 V vs RHE at a scan rate of 0.02 V s^{-1}.

Given the noted variation in catalytic current density with both film composition and phase behavior, there is no indication that the Pt conducting underlayer contributes meaningfully to the electrochemical characterization in Figures 1 and 2a, but given the importance of the Sb–Mn catalyst being free of precious metals, its activity was also validated by depositing a film on an FTO-coated glass substrate. This conducting layer limits the ability to characterize the catalyst thin film due to its interference with both XRF and XRD measurements, prompting our target of approximately x = 0.67 and annealing at 550 °C to provide sufficient XRD intensity to confirm that the film crystallized in the rutile structure (Figure S1). We performed 40 min of continuous CV cycling of the film, corresponding to 45 cycles as shown in Figure 2b. While some degradation is observed in the first few cycles, electrocatalytic activity is maintained over the course of the experiment, with the overpotential required to reach 10 mA cm^{-2} increasing by only 15 mV (from 508 to 523 mV) during the measurement.

3.2. Stability of Catalyst Activity and Composition. Further evaluation of operational stability was performed by operating larger samples in a traditional electrochemical H-cell with carbon counter electrode. A 1.75 cm^2 electrode containing FTO-supported $Mn_{0.70}Sb_{0.30}O_z$ (composition determined by ICP-MS) annealed at 550 °C was cycled between

DOI: 10.1021/acscatal.8b02689
ACS Catal. 2018, 8, 10938–10948

1.23 and 1.83 V vs RHE (uncompensated) at 0.02 V s^{-1}. Over the course of 4320 CV cycles, aliquots of electrolyte were extracted to quantify the dissolved concentrations of Sb and Mn via ICP-MS. The electrolyte was replaced after 6 h of testing to confirm that catalytic activity continued after returning the metal concentrations to near-zero. Similar experiments were performed on a Mn_2O_3 electrode for comparison, with measurements stopped after 40 cycles due to loss of activity. The results are summarized in Figure 3,

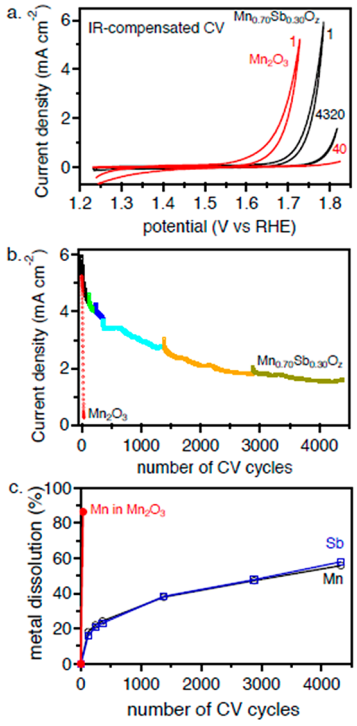

Figure 3. (a) IR-compensated CVs in 1.0 M H_2SO_4 solution between 1.23 and 1.83 V vs RHE at a rate of 0.02 V s^{-1} of two epoxy-encapsulated electrodes: $Mn_{0.70}Sb_{0.30}O_z$ and Mn_2O_3, which were both deposited on FTO and annealed at 550 °C (see Figure S16 for non-IR-compensated CVs). (b) Current density obtained at the maximum potential in each CV cycle for both $Mn_{0.70}Sb_{0.30}O_z$ and Mn_2O_3 electrodes. (c) Cumulative fraction of dissolved metals as determined by ICP-MS measurements of the electrolyte.

revealing that the initial high current density provided by Mn_2O_3 quickly decays due to corrosion of 87% of the deposited Mn within 40 CV cycles. The $Mn_{0.70}Sb_{0.30}O_z$ degrades much more slowly with loss of approximately half of the 170 nm film after 4000 cycles, which corresponds to loss of approximately 0.1 monolayer per cycle, which exposes a new catalyst surface that is likely similar to the as-synthesized catalyst. The ICP-MS measurements also included complete digestion of the Sb–Mn catalyst film after testing as well as testing of the counter electrode and electrolyte to confirm the absence of precious metals up to the detectability limit of ~1 ppb.

Stability measurements with less CV cycling were performed on a 0.22 cm^2 electrode containing Pt-supported $Mn_{0.67}Sb_{0.33}O_z$ (composition determined by XRF) annealed at 700 °C. In addition, an epoxy-encapsulated electrode of the Pt/Ti/SiO_2/Si substrate (0.34 cm^2) was fabricated as a control sample to confirm that the conductive Pt underlayer does not contribute to the electrochemical characterization of the Sb–Mn catalyst (see Figure S18). The series of CV, CA, chronopotentiometry (CP), and open circuit potentiometry (OCP) measurements performed on the Mn–Sb catalyst is summarized in Figure 4, including approximately 27 h of CA

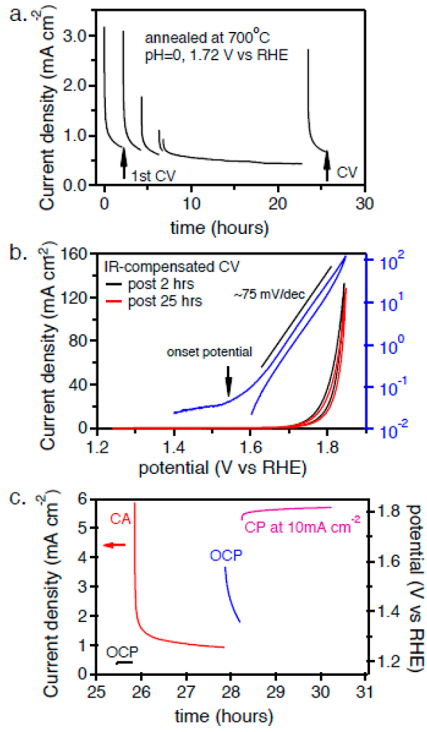

Figure 4. (a) Series of CA measurements at 1.72 V vs RHE (490 mV overpotential) in 1.0 M H_2SO_4 solution of epoxy-encapsulated rutile $Mn_{0.67}Sb_{0.33}O_z$ electrode annealed at 700 °C. (b) Two IR-compensated CVs at 0.01 V s^{-1} in between CA measurements: one is after 2 h, and the other is at the end of about 25 h of catalyst operation, which is also plotted in log-scale in blue color (see Figure S19 for non-IR-corrected CVs). (c) A subsequent batch of experiments on the same electrode where another 2 h CA measurement between two 20 min open circuit potential (OCP) measurements shows the decrease in current density during the CA is concurrent with an increase in the open circuit potential, which then "recovers" on the time scale of 10 min at open circuit. These measurements are followed by a 2 h chronopotentiometry (CP) measurement at current density of 10 mA cm^{-2} that is fairly stable at an overpotential of 586 mV for the final hour.

experiments at 1.72 V vs RHE along with two CV cycles acquired after both 2 and 25 h of CA measurements. The Sn-free electrode enabled quantification of elemental corrosion from XRF characterization of the film before and after electrochemical operation, as summarized in Figure S20 and Table S3, revealing substantially less corrosion than that observed in Figure 3c, with 3.8% of Sb and 25% of Mn corroded after approximately 30 h of electrochemical operation. This disparity in elemental corrosion from the 409 nm film indicates that the equivalent of ~5 nm of Sb oxide dissolves while Mn dissolves from at least 100 nm of as-synthesized film thickness, indicating that slow Mn corrosion proceeds via diffusion through an Sb-rich surface. The resistance-compensated CVs in Figure 4b reveal the excellent electrocatalytic activity with current density exceeding 50 mA cm^{-2} at 0.58 V overpotential. The low-current-density portion of the log-scale CV indicates that the onset of catalytic current is near 0.3 V overpotential, while the high-current-density

DOI: 10.1021/acscatal.8b02689
ACS Catal. 2018, 8, 10938–10948

Table 1. Analysis of the Total Anodic Charge from Stability Testing of a Mn Oxide and 3 Sb−Mn Oxide Electrodes[a]

as-synthesized composition	figure	conducting layer	anneal temp (°C)	CA + CP time (hours)	CV cycles	total charge (C)	O_2 per corroded Mn	O_2 per corroded Sb
Mn_1	3	FTO	550		40	0.872	2.0	
$Mn_{0.67}Sb_{0.33}$[b]	2	FTO	550		45	0.078	71	
$Mn_{0.70}Sb_{0.30}$	3	FTO	550		3240	19.444	86	1.9×10^2
$Mn_{0.67}Sb_{0.33}$	4	Pt	700	29	2	31.626	7.5×10^2	1.0×10^4

[a]Using XRF and/or ICP-MS to determine the dissolved Mn and Sb concentrations, and assuming 2 e^- per Mn and 1 e^- per Sb corrosion processes, the total OER charge was used to quantify the amount of O_2 produced, which was then divided by the respective number of corroded metal atoms. [b]This composition was not measured due to overlap of the XRF Sb peak with Sn peak from the FTO layer. The composition was estimated based on XRD data and comparisons to other libraries.

portion (0.1−100 mA cm^{-2}) shows a Tafel slope of about 75 mV dec^{-1}.

Figure 4a shows consistent current density above 0.5 mA cm^{-2} intermixed with a series of current transients which occur whenever the potentiostat is turned off to create an open circuit condition. When the open circuit duration is on the order of 1 min, the initial current density upon reapplication of the CA voltage is approximately 1 mA cm^{-2}; longer open circuit durations (40 min) restore the current density to approximately the initial value of 3 mA cm^{-2}. To further probe these phenomena, Figure 4c contains additional experiments starting with a 20 min OCP measurement which reveals that upon introduction to the electrolyte the open circuit potential is near the OER Nernstian potential. After a 2 h CA at 1.72 V vs RHE, the subsequent 20 min OCP starts at a higher value that decreases on the scale of 10 min; this change in OCP indicates a change to the catalyst surface that is responsible for the initial transients in activity for each CA measurement in Figure 4a,c. While this ability to recover activity at open circuit seems desirable, the deployment of this catalyst to attain stable OER operation hinges upon understanding the mechanism of current density restoration, particularly given the observation from Figure 3b that voltage cycling accelerates Sb and Mn dissolution.

To better quantify the differences in stability both between Mn_2O_3 and the Mn−Sb oxide alloy and between CV cycling and operation at more static potential, the total charge passed during respective measurements was compared with the amount of corroded Mn and Sb to determine the number of OER turnovers (4 e^- per O_2) per corroded Mn (assumed 2 e^- per Mn, see the SI) and per corroded Sb (assumed 1 e^- per Sb, see the SI). This quantity is similar to the turnover number (not turnover frequency) indicating the number of catalytic cycles before deactivation. The results in Table 1 demonstrate that the Mn−Sb catalyst provides a 40-fold improvement over Mn_2O_3 in the generated O_2 per corroded Mn ion during CV cycling. The catalyst operated primarily under CA and CP modes exhibits an additional ∼100-fold improvement, although notably this sample also differs in its substrate and annealing temperature. The low Sb corrosion during this measurement results in 10^4 O_2 per corroded Sb. The stoichiometric phase $MnSb_2O_6$, corresponding to the x = 0.33 sample in this work, was recently reported as an OER catalyst in 1.0 M H_2SO_4 electrolyte, and 60% Mn loss was observed over 168 h of CP operation,[16d] indicating that substantial Mn loss also occurs in Sb-rich compositions and motivating more detailed assessment of the thermodynamics of Mn−Sb rutile oxides.

3.3. Computational Assessment of Solid State and Aqueous Stability. Computational assessment of Mn−Sb rutile oxides commenced with solid-state stability as a function of alloy composition, particularly because the rutile phase has only been previously observed at Mn concentrations up to $Mn_{0.5}Sb_{0.5}O_2$,[32] so our observation of continued alloying up to x = 0.70 constitutes the discovery of new phase behavior in this composition space. To evaluate the phase stability of rutile alloys, supercells containing 6 cation sites were populated with Sb and/or Mn to create a series of 7 compositions: x = 0, 1/6, 1/3, 1/2, 2/3, 5/6, and 1. A 2 × 2 × 2 supercell of rutile TiO_2 (substituted at x = 1/2 to form $MnSbO_4$) is also considered as a template, with compositional perturbations yielding structures with formula $Mn_xSb_{1-x}O_2$ where x = 3/8, 7/16, 1/2, 9/16, and 5/8. The formation energy (ΔE_{form}) for each phase is shown in Figure 5 along with the nonrutile phases

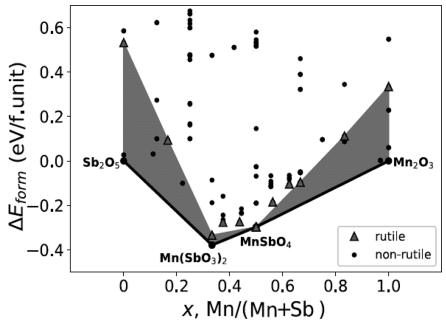

Figure 5. Grand potential phase diagram: calculated formation energy (ΔE_{form}) variation with the composition for phases in Mn−Sb−O system at 700 °C and 0.2 atm O_2, in addition to the rutile structure TiO_2 and trirutile $CoSb_2O_6$. The rutile and nonrutile phases are indicated with green triangles and black circles, respectively. The nonrutile phases in Mn−Sb−O system are provided in Figure S21, SI. The shaded region indicates the above-hull energy of the rutile structures.

from the Materials Project database, revealing that a rutile alloy lies on the convex hull only at x = 1/2. At x = 1/3, the hexagonal phase $MnSb_2O_6$ is energetically more favorable with formation energy only 20 meV (formula unit)$^{-1}$ below the rutile structure, which is well within the characteristic 80 meV (formula unit)$^{-1}$ window of the generalized-gradient-based (GGA-based) above-hull energy where most synthesizable phases are found.[33] Rutile alloys exist in this 80 meV (formula unit)$^{-1}$ above-hull window from approximately x = 1/3, which matches our experimental observation of the rutile alloy phase boundary with 700 °C annealing, to approximately x = 2/3, which is in good agreement with our experimental value of x = 0.70.

This series of rutile oxide alloys also enables evaluation of the thermodynamic enhancement in Mn stability provided by the Sb−Mn rutile oxide (Figure 3 and Table 1). Stability

DOI: 10.1021/acscatal.8b02689
ACS Catal. 2018, 8, 10938−10948

analysis for OER conditions in strong acid was assessed with Pourbaix calculations using the recently developed formalism for calculating the above-hull energy for a given material as a function of pH and potential.[28b] Figure 6a shows the calculated

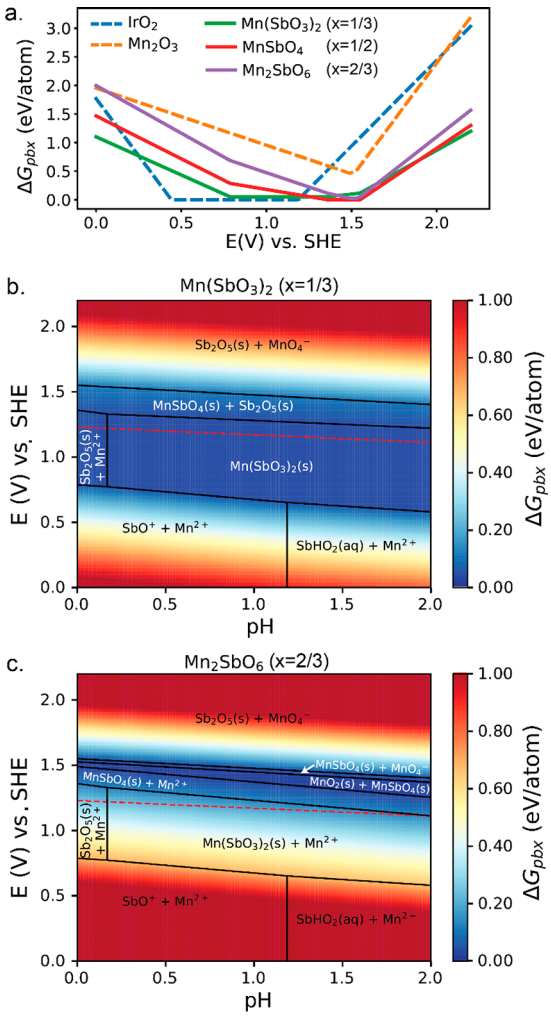

Figure 6. (a) Calculated Gibbs free energy above hull at pH 0 for 3 Mn−Sb rutile alloys at x = 1/3, 1/2, and 2/3, respectively, along with Mn_2O_3 and IrO_2 as comparison in the potential range 0−2.2 V vs SHE. The moderate overpotential portion of Pourbaix above-hull energy reveals that all 3 Mn−Sb rutile alloys are more thermodynamically stable than IrO_2 in strong acid. Computationally predicted Pourbaix diagram of Sb−Mn−O system at pH = 0−2 range for Mn content (b) x = 1/3 and (c) x = 2/3, respectively. The Mn and Sb ion concentrations each fixed at 10^{-9} M. The Gibbs free energy (ΔG_{pbx}) of the rutile $MnSb_2O_6$ and Mn_2SbO_6 with respect to the Pourbaix stable phases is superimposed on the corresponding Pourbaix diagram and represented by the color bar. The red dashed lines denote potential of 1.23 V vs RHE (OER potential).

Pourbaix above-hull energies at pH 0 for 3 Mn−Sb rutile alloys (with composition of x = 1/3, 1/2, and 2/3), revealing that all three Mn−Sb compositions ($MnSb_2O_6$, $MnSbO_4$, and Mn_2SbO_6) are thermodynamically more stable than IrO_2 in strong acid at moderate overpotential, although these results do not account for any differences in corrosion kinetics. Since the Mn−Sb catalysts need to be operated at higher overpotentials, the energy above hull at OER operation is similar for IrO_2 and these precious-metal-free catalysts.

Figure 6b,c contains the resulting Pourbaix above-hull energy for the trirutile phase $MnSb_2O_6$ (x = 1/3) and the rutile alloy Mn_2SbO_6 (x = 2/3) with Mn and Sb ion concentrations each fixed at 10^{-9} M. The corresponding Pourbaix diagrams show that the x = 1/2 rutile alloy $MnSbO_4$ is thermodynamically stable in strong acid for moderate OER overpotentials. Since the Mn-rich alloys from the solid-state stability analysis of Figure 5 do not lie on the convex hull of ΔE_{form}, they cannot appear in the Pourbaix hull and thus cannot appear in the Pourbaix diagram. Figure 6c shows that, at 1.5 V vs RHE, just below the OER onset potential noted above, Mn_2SbO_6 has a small driving force for decomposing into $MnSbO_4$ and MnO_2 solids, which arises only from the difference in ΔE_{form} shown in Figure 5 and indicates that no corrosion will occur under these electrochemical conditions. At higher and lower OER potentials, the Pourbaix analysis predicts that Mn will corrode as MnO_4^- and Mn^{2+}, respectively, indicating that substantially improved stability may be obtained through catalyst optimization to slightly lower the onset potential and enable stable operation under tight potential control.

The Pourbaix analysis of Figure 6 also indicates that, under the potential range of the CVs in Figures 2−4, Sb is thermodynamically stable, in contradiction to the observed Sb dissolution under CV cycling. The corrosion curves of Figure 3c demonstrate that Sb and Mn are dissolved in proportion to the film composition. With no candidate electrochemical pathways for this dissolution, this degradation may be mechanical in nature, which we explore by calculating the Sb-atom normalized ratios between the volumes of Sb_2O_5 and $Mn_xSb_{1-x}O_6$. These values, analogous to the Pilling−Bedworth ratios, are 0.89, 0.76, and 0.57 for x = 1/3, 1/2, and 2/3, respectively, and suggest that corroding Mn from the near-surface will create increasing compressive strain with increasing Mn in the as-synthesized film material, which makes the Mn-rich compositions more susceptible to any mechanical degradation that is triggered by CV cycling. This possibility of mechanical degradation not only highlights the importance of optimizing catalyst morphology in future development, but also underscores the difference in degradation during CV cycling compared to the diffusion-limited Mn corrosion that occurs during catalyst operation at appreciable overpotential.

Another key observation from Figure 6a is that, under OER potentials, the Sb−Mn rutile oxides are more stable than Mn_2O_3 by 0.5−1 eV atom^{-1}. Considering that Sb_2O_5 is stable under these conditions, this thermodynamic stabilization can be viewed as a stabilization of the Mn, motivating investigation of the presence of low-valent Mn in the Mn−Sb rutile oxide catalyst, which is pursued below.

3.4. Identification of Low-Valent Mn and Its Mechanistic Importance. Characterization of the ionic composition of the Mn−Sb rutile oxides commenced with XAS characterization of 4 samples after the 200 s CA measurements in Figure 2a (postelectrochemistry samples), as well as 4 as-synthesized samples with x = 0.35, 0.38, 0.53, and 0.69. As seen in Figure 7a, there is no measurable change of Sb K-edge signal over the range of composition measured, and the Sb XAS signal is unaffected by the 200 s CA measurement, corroborating the electrochemical stability of Sb. All of the Sb K-edge spectra match well with the reference of Sb_2O_5 indicating that Sb is present as Sb^{5+} across the entire composition range of rutile alloy $Mn_xSb_{1-x}O_z$. More variability is observed in the Mn XAS signals (Figure 7b), and importantly the variability is primarily

DOI: 10.1021/acscatal.8b02689
ACS Catal. 2018, 8, 10938−10948

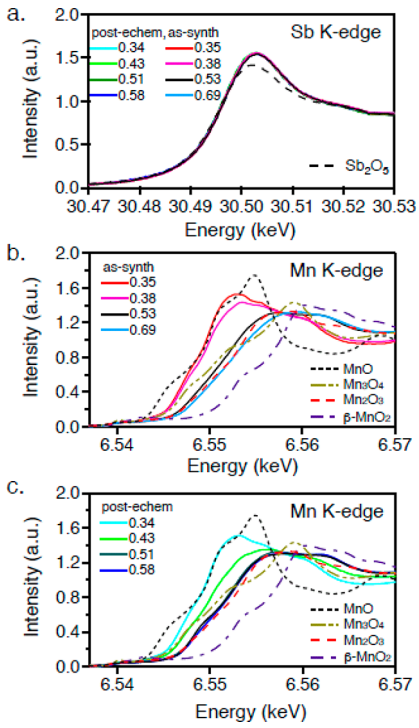

Figure 7. (a) Sb and (b, c) Mn K-edge XAS spectra of rutile alloy $Mn_xSb_{1-x}O_z$ at a series of Mn concentrations for both as-synthesized and postelectrochemistry films. The reference antimony and manganese oxides with known oxidation states are shown in dashed lines.

a function of as-synthesized composition and not introduced by the 200 s CA measurement. This indicates that while some Mn corrodes from the film, the remaining Mn does not experience any irreversible electrochemical oxidation during catalyst operation. Each Mn K-edge spectrum exhibits an absorption edge energy that increases with Mn concentration in the rutile alloy but remains between that of the Mn^{2+} and Mn^{3+} reference spectra, corresponding to an increase in the average Mn oxidation state with increasing x, as shown in Figure 8.

If the rutile alloy maintains a 2 oxygen per cation stoichiometry, and the O and Sb remain in their respective −2 and +5 formal oxidation states, charge balance requires the average oxidation state of Mn in $Mn_xSb_{1-x}O_2$ alloy to be $5 - x^{-1}$, as shown in Figure 8. At x = 1/3, this gives the Mn^{2+}

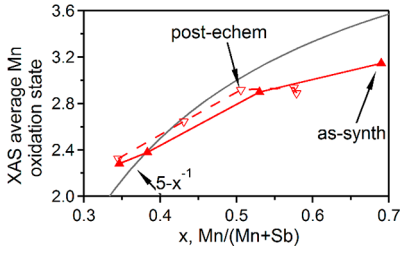

Figure 8. Average Mn oxidation state derived from XAS measurements for both as-synthesized and postelectrochemistry films, showing a marked increase in Mn oxidation state with increasing Mn concentration. The formal Mn oxidation state corresponding to y in $Mn^y{}_xSb^{5+}{}_{1-x}O^{2-}{}_2$ is also shown in gray. Note that the post-electrochemistry samples are plotted according to their post-electrochemistry XRF values of x.

reported[32a] to exist in the trirutile $MnSb_2O_6$ and predicts that the average Mn oxidation state would exceed +3 within our observed rutile alloy composition window. While the XAS results share the qualitative behavior of increasing Mn oxidation with increasing Mn concentration, which is further corroborated by Bader charge analysis of the computational structures (Figure S14), the +3 value is only reached at the phase boundary of the Mn-saturated rutile alloy and Mn_2O_3.

The low average Mn oxidation state at high Mn concentrations suggests that the Mn-rich rutile alloys exhibit some combination of O vacancies and/or covalent Mn−O bonding that corresponds to deviations from the formal integer valences. The formation energy for an O vacancy was evaluated with supercell calculations (Figure S22) revealing above-hull energies as low as 0.16 eV (formula unit)$^{-1}$ near x = 0.5 with higher above-hull energies at both Mn-rich and Sb-rich rutile oxide compositions, which does not plausibly explain the observations of Figure 8 considering that balancing charge for the Mn-rich compositions would require about 10% of O^{2-} sites to be vacant. Analysis of the relative Bader charge for O in the rutile oxide supercells (Figure S14) reveals that its absolute value decreases and becomes more variable over the 12 supercell sites as the Mn concentration increases, which is an indicator of increasing Mn−O covalency in the Mn-rich rutile oxide alloys. Formation of Mn^{4+} would enabled more ionic bonding, and some intuition for the absence of this phenomenon can be gained from analysis of ionic radii considering that Mn^{4+} has about 10% lower ionic radius than the approximately equal radii of Sb^{5+} and Mn^{3+}.[34] To further characterize the Mn−O bonds, we return to the XAS characterization where the Mn−K extended X-ray absorption fine structure (EXAFS) signals were generated for the most Sb-rich and Mn-rich as-synthesized samples from Figure 7 and analyzed by fitting the first coordination shell (Figure S12). For x = 0.35, the fitted Mn−O bond distance for MnO_6 octahedra was 2.13 Å, whereas two Mn−O bond distances (approximately 1.9 and 2.2 Å) were required to fit the EXAFS data at x = 0.72. This variation in the Mn−O bond distance is in good agreement with the supercell rutile model at x = 0.67, which has ∼3% larger volume due to 3% larger value of the c lattice parameter compared to experiment (see Figure S13). In this 18 atom supercell, the Mn−O distances range from 1.93 to 2.04 Å, and the Mn−Mn nearest neighbor distances vary from 2.97 to 3.56 Å. Collectively, these results are consistent with Jahn−Teller distortions that are common to Mn^{3+} oxides and indicate that the catalyst contains a mixture of edge-sharing and corner-sharing $Mn^{3+}O_6$ octahedra.[20,36]

While the Pourbaix analysis combined with XAS analysis highlights the stabilization of Mn^{3+} under OER conditions in the Sb−Mn catalyst, direct observation of surface species during catalyst operation is notoriously difficult. We performed the related measurement of XPS analysis of the near-surface chemistry after OER operation, both in vacuum and under exposure to H_2O, the latter measurement enabled by recent development of ambient pressure XPS (AP-XPS).[30] An electrode similar to that of Figure 3 was cycled 50 times between 1.23 and 1.83 V vs RHE (same as Figure 3) and subsequently cut from the epoxy-sealed electrode for XPS analysis. The survey scan in Figure 9a shows approximately equal concentrations of Sb and Mn in the near-surface region. The measurement was also performed on an as-synthesized Mn_2O_3 film to enable comparison of the Mn oxidation state. The inset shows the Mn 3s doublet from each material, and the

DOI: 10.1021/acscatal.8b02689
ACS Catal. 2018, 8, 10938−10948

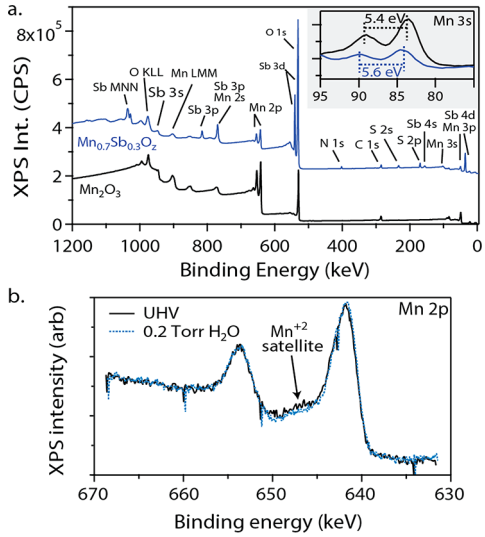

Figure 9. XPS analysis of a Mn_2O_3 film (as-synthesized) and $Mn_{0.70}Sb_{0.30}O_z$ sample after 50 CVs in 1 M H_2SO_4 (see Figure S15). (a) Survey scan shows the as-synthesized elements as well as S from the electrolyte. Analysis of the Mn 2p and Sb $3d_{3/2}$ signals indicates the near-surface Mn:Sb is approximately 1:1. The inset shows the Mn 3s signal from both films, where the larger peak splitting in the Sb–Mn film is due to the presence of Mn^{2+}. (b) Using AP-XPS, Mn 2p spectra on the $Mn_{0.70}Sb_{0.30}O_z$ sample reveal the presence of the Mn^{2+} satellite feature, indicating a mixture of Mn^{2+} and Mn^{3+} in the near-surface. The intensity of the satellite feature is lower upon exposure to 0.2 Torr H_2O but still present, demonstrating oxidation resistance of the Sb–Mn film.

5.4 eV peak splitting for the Mn_2O_3 film is just below the literature value of 5.5 eV[35] for Mn^{3+}, indicating an average oxidation state above +3. The higher 5.6 eV splitting from the postelectrochemistry Mn–Sb catalyst indicates an average oxidation state below +3 (literature value for Mn^{2+} peak splitting is 5.9 eV), demonstrating that the mixture of Mn^{2+} and Mn^{3+} in the bulk (Figures 7 and 8) also appears in the near-surface region, likely with a higher prevalence of Mn^{3+}. To assess whether this mixture of Mn^{2+} and Mn^{3+} oxidizes upon water exposure, AP-XPS of the Mn 2p region was performed in 0.2 Torr H_2O where the signal appeared stable over 90 min of water exposure. Figure 9b compares this signal to that measured in vacuum before water exposure. While the Mn 2p peak positions for Mn^{2+} and Mn^{3+} are similar, the distinguishing feature of Mn^{2+} is a satellite feature that is observed in the vacuum measurement and still observed with somewhat lower intensity upon water exposure. There is no indication of oxidation to Mn^{4+}, with these results corroborating the Pourbaix and XAS analysis that Mn^{2+} and Mn^{3+} exist in the near-surface region and are resistant to oxidation.

The OER environment is more oxidizing than the AP-XPS environment, making the Pourbaix analysis the most definitive characterization of stable Mn species, from which the 0.5–1 eV $atom^{-1}$ stabilization of Mn^{3+} is the most distinguishing feature of the Mn–Sb rutile oxides, which is in excellent agreement with present understanding of the importance of Mn^{3+} in catalyzing the OER.[20b,21,36] Mn^{3+} octahedra, both in corner-sharing and edge-sharing configurations, have been established as the predominant active species through extensive analysis of Mn oxide and hydroxide OER catalysts.[20,36] As noted above, the Mn-rich rutile oxides have both corner- and edge-sharing octahedral, which explains why stabilization of Mn^{3+} is critical for realizing its OER activity in strong acid. The increasing Mn–O covalency in the Mn-rich rutile oxide alloys, which exhibit the highest activity, is in excellent agreement with previous analysis of electrochemically activated Mn^{3+} in acid, for which the OER activity is attributed to a reduction in the HOMO–LUMO gap that increases the metal–oxygen covalency and therefore increases the equilibrium concentration of reactive oxyl radical species.[21,37] Through analysis of variation in OER reaction mechanism with electronic structure of transition-metal oxides (including multimetal oxides), the metal–oxygen covalency was determined to be a key differentiator between the conventional coupled electron–proton transfer mechanism and a mechanism in which nonconcerted proton–electron transfer is coupled to lattice oxygen activation.[38] The increased Mn–O covalency of the Mn-rich rutile oxides, as identified by Bader charge and XAS analyses, indicates that OER proceeds via the nonconcerted mechanism on the Mn–Sb rutile oxides, which explains the sharp increase in activity with increasing Mn concentration and crystallization into the rutile structure (Figure 1).

4. CONCLUSIONS

Stable oxygen evolution catalysis in strong acid electrolyte poses substantial challenges for non-precious-metal electrocatalysts, with Mn oxide species able to provide substantial activity if incorporated in an environment that stabilizes Mn^{3+}. We show that such stabilization is provided by alloying Mn into a $(Sb,Mn)O_2$ rutile structure, in particular with Mn-rich alloys that are reported here for the first time and supported by extensive DFT calculations including Pourbaix analysis that highlights the role of Sb and the rutile structure in stabilizing Mn^{3+} under OER conditions in acid. Characterization of the alloys by synchrotron X-ray absorption spectroscopy, which is supported by AP-XPS and computational analysis, reveals an increase in Mn^{3+} concentration as well as Mn–O covalency with increasing Mn content in the alloy, both of which increase OER activity and make these manganese antimonates the most promising electrocatalysts for water electrolysis in acidic media without precious metals.

■ ASSOCIATED CONTENT

Supporting Information

The Supporting Information is available free of charge on the ACS Publications website at DOI: 10.1021/acscatal.8b02689.

Experimental and computational details, additional electrochemical and materials characterization data and figures including current density, CA measurements, XRD plots, CV curves, metal loading, nominal film thickness, EXAFS spectra, lattice parameters, Bader charge analysis, EIS Bode plot, XRF spectra, grand potential phase diagrams, and Pourbaix diagrams (PDF)

■ AUTHOR INFORMATION

Corresponding Authors

*E-mail: kapersson@lbl.gov.
*E-mail: gregoire@caltech.edu.

ORCID

Aniketa Shinde: 0000-0003-2386-3848
Junko Yano: 0000-0001-6308-9071
Ethan J. Crumlin: 0000-0003-3132-190X
Matthias H. Richter: 0000-0003-0091-2045

DOI: 10.1021/acscatal.8b02689
ACS Catal. 2018, 8, 10938–10948

Jason K. Cooper: 0000-0002-7953-4229
Joel A. Haber: 0000-0001-7847-5506
Kristin A. Persson: 0000-0003-2495-5509
John M. Gregoire: 0000-0002-2863-5265

Notes

The authors declare no competing financial interest.

■ ACKNOWLEDGMENTS

This study is based upon work performed by the Joint Center for Artificial Photosynthesis, a DOE Energy Innovation Hub, supported through the Office of Science of the U.S. Department of Energy (Award DE-SC0004993). Computational work was additionally supported by the Materials Project Program (Grant KC23MP) through the DOE Office of Basic Energy Sciences, Materials Sciences and Engineering Division, under Contract DE-AC02-05CH11231. Computational resources were provided by the National Energy Research Scientific Computing Center, a DOE Office of Science User Facility supported by the Office of Science of the DOE under Contract DE-AC02-05CH11231. Part of this work (XAS data collection) was carried out at Stanford Synchrotron Radiation Lightsource, SLAC National Accelerator Laboratory, supported by the U.S. Department of Energy, Office of Science, Office of Basic Energy Sciences under Contract DE-AC02-76SF00515. XAS studies were performed with support of the Office of Science, OBES, Division of Chemical Sciences, Geosciences, and Biosciences (CSGB) of the DOE under Contract DE-AC02-05CH11231 (J. Yano). AP-XPS was carried out at Advanced Light Source, Lawrence Berkeley National Laboratory, supported by the U.S. Department of Energy, Office of Science, Office of Basic Energy Sciences under Contract DE-AC02-05CH11231. We acknowledge support from the Beckman Institute of the California Institute of Technology to the Molecular Materials Research Center that enabled vacuum XPS characterization.

■ REFERENCES

(1) (a) McKone, J. R.; Lewis, N. S.; Gray, H. B. Will Solar-Driven Water-Splitting Devices See the Light of Day? *Chem. Mater.* **2014**, *26* (1), 407−414. (b) Reier, T.; Nong Hong, N.; Teschner, D.; Schlögl, R.; Strasser, P. Electrocatalytic Oxygen Evolution Reaction in Acidic Environments - Reaction Mechanisms and Catalysts. *Adv. Energy Mater.* **2017**, *7* (1), 1601275.

(2) Walter, M. G.; Warren, E. L.; McKone, J. R.; Boettcher, S. W.; Mi, Q.; Santori, E. A.; Lewis, N. S. Solar Water Splitting Cells. *Chem. Rev.* **2010**, *110* (11), 6446−6473.

(3) McCrory, C. C. L.; Jung, S.; Ferrer, I. M.; Chatman, S. M.; Peters, J. C.; Jaramillo, T. F. Benchmarking Hydrogen Evolving Reaction and Oxygen Evolving Reaction Electrocatalysts for Solar Water Splitting Devices. *J. Am. Chem. Soc.* **2015**, *137* (13), 4347−4357.

(4) (a) Xiang, C.; Weber, A. Z.; Ardo, S.; Berger, A.; Chen, Y.; Coridan, R.; Fountaine, K. T.; Haussener, S.; Hu, S.; Liu, R.; Lewis, N. S.; Modestino, M. A.; Shaner, M. M.; Singh, M. R.; Stevens, J. C.; Sun, K.; Walczak, K. Modeling, Simulation, and Implementation of Solar-Driven Water-Splitting Devices. *Angew. Chem., Int. Ed.* **2016**, *55* (42), 12974−12988. (b) Jin, J.; Walczak, K.; Singh, M. R.; Karp, C.; Lewis, N. S.; Xiang, C. An experimental and modeling/simulation-based evaluation of the efficiency and operational performance characteristics of an integrated, membrane-free, neutral pH solar-driven water-splitting system. *Energy Environ. Sci.* **2014**, *7* (10), 3371−3380. (c) Singh, M. R.; Papadantonakis, K.; Xiang, C.; Lewis, N. S. An electrochemical engineering assessment of the operational conditions and constraints for solar-driven water-splitting systems at near-neutral pH. *Energy Environ. Sci.* **2015**, *8* (9), 2760−2767.

(5) Kumari, S.; Ajayi, B. P.; Kumar, B.; Jasinski, J. B.; Sunkara, M. K.; Spurgeon, J. M. A low-noble-metal $W_{1-x}Ir_xO_{3-\delta}$ water oxidation electrocatalyst for acidic media via rapid plasma synthesis. *Energy Environ. Sci.* **2017**, *10* (11), 2432−2440.

(6) Gaudet, J.; Tavares, A. C.; Trasatti, S.; Guay, D. Physicochemical Characterization of Mixed RuO_2-SnO_2 Solid Solutions. *Chem. Mater.* **2005**, *17* (6), 1570−1579.

(7) Pérez-Viramontes, N. J.; Escalante-García, I. L.; Guzmán-Martínez, C.; Galván-Valencia, M.; Durón-Torres, S. M. Electrochemical study of Ir-Sn-Sb-O materials as catalyst-supports for the oxygen evolution reaction. *J. Appl. Electrochem.* **2015**, *45* (11), 1165−1173.

(8) Kadakia, K.; Datta, M. K.; Velikokhatnyi, O. I.; Jampani, P.; Park, S. K.; Saha, P.; Poston, J. A.; Manivannan, A.; Kumta, P. N. Novel $(Ir,Sn,Nb)O_2$ anode electrocatalysts with reduced noble metal content for PEM based water electrolysis. *Int. J. Hydrogen Energy* **2012**, *37* (4), 3001−3013.

(9) Sun, W.; Cao, L.-m.; Yang, J. Conversion of inert cryptomelane-type manganese oxide into a highly efficient oxygen evolution catalyst via limited Ir doping. *J. Mater. Chem. A* **2016**, *4* (32), 12561−12570.

(10) Oakton, E.; Lebedev, D.; Povia, M.; Abbott, D. F.; Fabbri, E.; Fedorov, A.; Nachtegaal, M.; Copéret, C.; Schmidt, T. J. IrO_2-TiO_2: A High-Surface-Area, Active, and Stable Electrocatalyst for the Oxygen Evolution Reaction. *ACS Catal.* **2017**, *7* (4), 2346−2352.

(11) Marshall, A. T.; Sunde, S.; Tsypkin, M.; Tunold, R. Performance of a PEM water electrolysis cell using $Ir_xRu_yTa_zO_2$ electrocatalysts for the oxygen evolution electrode. *Int. J. Hydrogen Energy* **2007**, *32* (13), 2320−2324.

(12) (a) Macounová, K.; Jirkovský, J.; Makarova, M. V.; Franc, J.; Krtil, P. Oxygen evolution on $Ru_{1-x}Ni_xO_{2-y}$ nanocrystalline electrodes. *J. Solid State Electrochem.* **2009**, *13* (6), 959−965. (b) Reier, T.; Pawolek, Z.; Cherevko, S.; Bruns, M.; Jones, T.; Teschner, D.; Selve, S.; Bergmann, A.; Nong, H. N.; Schlögl, R.; Mayrhofer, K. J. J.; Strasser, P. Molecular Insight in Structure and Activity of Highly Efficient, Low-Ir Ir-Ni Oxide Catalysts for Electrochemical Water Splitting (OER). *J. Am. Chem. Soc.* **2015**, *137* (40), 13031−13040.

(13) Tae, E. L.; Song, J.; Lee, A. R.; Kim, C. H.; Yoon, S.; Hwang, I. C.; Kim, M. G.; Yoon, K. B. Cobalt Oxide Electrode Doped with Iridium Oxide as Highly Efficient Water Oxidation Electrode. *ACS Catal.* **2015**, *5* (9), 5525−5529.

(14) (a) Mondschein, J. S.; Callejas, J. F.; Read, C. G.; Chen, J. Y. C.; Holder, C. F.; Badding, C. K.; Schaak, R. E. Crystalline Cobalt Oxide Films for Sustained Electrocatalytic Oxygen Evolution under Strongly Acidic Conditions. *Chem. Mater.* **2017**, *29* (3), 950−957. (b) Blasco-Ahicart, M.; Soriano-López, J.; Carbó, J. J.; Poblet, J. M.; Galan-Mascaros, J. R. Polyoxometalate electrocatalysts based on earth-abundant metals for efficient water oxidation in acidic media. *Nat. Chem.* **2017**, *10*, 24. (c) Yang, X.; Li, H.; Lu, A.-Y.; Min, S.; Idriss, Z.; Hedhili, M. N.; Huang, K.-W.; Idriss, H.; Li, L.-J. Highly acid-durable carbon coated Co_3O_4 nanoarrays as efficient oxygen evolution electrocatalysts. *Nano Energy* **2016**, *25*, 42−50. (d) Yan, K.-L.; Chi, J.-Q.; Xie, J.-Y.; Dong, B.; Liu, Z.-Z.; Gao, W.-K.; Lin, J.-H.; Chai, Y.-M.; Liu, C.-G. Mesoporous Ag-doped Co_3O_4 nanowire arrays supported on FTO as efficient electrocatalysts for oxygen evolution reaction in acidic media. *Renewable Energy* **2018**, *119*, 54−61. (e) Yan, K.-L.; Qin, J.-F.; Lin, J.-H.; Dong, B.; Chi, J.-Q.; Liu, Z.-Z.; Dai, F.-N.; Chai, Y.-M.; Liu, C.-G. Probing the active sites of Co_3O_4 for the acidic oxygen evolution reaction by modulating the Co^{2+}/Co^{3+} ratio. *J. Mater. Chem. A* **2018**, *6* (14), 5678−5686.

(15) Kwong, W. L.; Lee, C. C.; Shchukarev, A.; Björn, E.; Messinger, J. High-performance iron (III) oxide electrocatalyst for water oxidation in strongly acidic media. *J. Catal.* **2018**, *365*, 29−35.

(16) (a) Shinde, A.; Jones, R. J. R.; Guevarra, D.; Mitrovic, S.; Becerra-Stasiewicz, N.; Haber, J. A.; Jin, J.; Gregoire, J. M. High-Throughput Screening for Acid-Stable Oxygen Evolution Electrocatalysts in the $(Mn-Co-Ta-Sb)O_x$ Composition Space. *Electrocatalysis* **2015**, *6* (2), 229−236. (b) Huynh, M.; Ozel, T.; Liu, C.; Lau, E. C.;

DOI: 10.1021/acscatal.8b02689
ACS Catal. 2018, 8, 10938−10948

Nocera, D. G. Design of template-stabilized active and earth-abundant oxygen evolution catalysts in acid. *Chem. Sci.* **2017**, *8* (7), 4779−4794. (c) Patel, P. P.; Datta, M. K.; Velikokhatnyi, O. I.; Kuruba, R.; Damodaran, K.; Jampani, P.; Gattu, B.; Shanthi, P. M.; Damle, S. S.; Kumta, P. N. Noble metal-free bifunctional oxygen evolution and oxygen reduction acidic media electro-catalysts. *Sci. Rep.* **2016**, *6*, 28367. (d) Moreno-Hernandez, I. A.; MacFarland, C. A.; Read, C. G.; Papadantonakis, K. M.; Brunschwig, B. S.; Lewis, N. S. Crystalline nickel manganese antimonate as a stable water-oxidation catalyst in aqueous 1.0 M H_2SO_4. *Energy Environ. Sci.* **2017**, *10* (10), 2103−2108. (e) Frydendal, R.; Paoli, E. A.; Chorkendorff, I.; Rossmeisl, J.; Stephens, I. E. L. Toward an Active and Stable Catalyst for Oxygen Evolution in Acidic Media: Ti-Stabilized MnO_2. *Adv. Energy Mater.* **2015**, *5* (22), 1500991.

(17) Post, J. E. Manganese oxide minerals: Crystal structures and economic and environmental significance. *Proc. Natl. Acad. Sci. U. S. A.* **1999**, *96* (7), 3447−3454.

(18) Takashima, T.; Hashimoto, K.; Nakamura, R. Mechanisms of pH-Dependent Activity for Water Oxidation to Molecular Oxygen by MnO_2 Electrocatalysts. *J. Am. Chem. Soc.* **2012**, *134* (3), 1519−1527.

(19) Takashima, T.; Hashimoto, K.; Nakamura, R. Inhibition of Charge Disproportionation of MnO_2 Electrocatalysts for Efficient Water Oxidation under Neutral Conditions. *J. Am. Chem. Soc.* **2012**, *134* (44), 18153−18156.

(20) (a) Zaharieva, I.; Chernev, P.; Risch, M.; Klingan, K.; Kohlhoff, M.; Fischer, A.; Dau, H. Electrosynthesis, functional, and structural characterization of a water-oxidizing manganese oxide. *Energy Environ. Sci.* **2012**, *5* (5), 7081−7089. (b) Gorlin, Y.; Lassalle-Kaiser, B.; Benck, J. D.; Gul, S.; Webb, S. M.; Yachandra, V. K.; Yano, J.; Jaramillo, T. F. In Situ X-ray Absorption Spectroscopy Investigation of a Bifunctional Manganese Oxide Catalyst with High Activity for Electrochemical Water Oxidation and Oxygen Reduction. *J. Am. Chem. Soc.* **2013**, *135* (23), 8525−8534. (c) Huynh, M.; Shi, C.; Billinge, S. J. L.; Nocera, D. G. Nature of Activated Manganese Oxide for Oxygen Evolution. *J. Am. Chem. Soc.* **2015**, *137* (47), 14887−14904.

(21) Morgan Chan, Z.; Kitchaev, D. A.; Nelson Weker, J.; Schnedermann, C.; Lim, K.; Ceder, G.; Tumas, W.; Toney, M. F.; Nocera, D. G. Electrochemical trapping of metastable Mn^{3+} ions for activation of MnO_2 oxygen evolution catalysts. *Proc. Natl. Acad. Sci. U. S. A.* **2018**, *115* (23), E5261−E5268.

(22) Oh, H. S.; Nong Hong, N.; Strasser, P. Preparation of Mesoporous Sb-, F-, and In-Doped SnO_2 Bulk Powder with High Surface Area for Use as Catalyst Supports in Electrolytic Cells. *Adv. Funct. Mater.* **2015**, *25* (7), 1074−1081.

(23) Seley, D.; Ayers, K.; Parkinson, B. A. Combinatorial Search for Improved Metal Oxide Oxygen Evolution Electrocatalysts in Acidic Electrolytes. *ACS Comb. Sci.* **2013**, *15* (2), 82−89.

(24) Suram, S. K.; Zhou, L.; Becerra-Stasiewicz, N.; Kan, K.; Jones, R. J. R.; Kendrick, B. M.; Gregoire, J. M. Combinatorial thin film composition mapping using three dimensional deposition profiles. *Rev. Sci. Instrum.* **2015**, *86* (3), 033904.

(25) Gregoire, J. M.; Xiang, C.; Liu, X.; Marcin, M.; Jin, J. Scanning droplet cell for high throughput electrochemical and photoelectrochemical measurements. *Rev. Sci. Instrum.* **2013**, *84* (2), 024102.

(26) Jain, A.; Ong, S. P.; Hautier, G.; Chen, W.; Richards, W. D.; Dacek, S.; Cholia, S.; Gunter, D.; Skinner, D.; Ceder, G.; Persson, K. A. Commentary: The Materials Project: A materials genome approach to accelerating materials innovation. *APL Mater.* **2013**, *1* (1), 011002.

(27) (a) Kresse, G.; Hafner, J. Ab initio molecular dynamics for liquid metals. *Phys. Rev. B: Condens. Matter Mater. Phys.* **1993**, *47* (1), 558−561. (b) Kresse, G.; Furthmüller, J. Efficiency of ab-initio total energy calculations for metals and semiconductors using a plane-wave basis set. *Comput. Mater. Sci.* **1996**, *6* (1), 15−50. (c) Kresse, G.; Furthmüller, J. Efficient iterative schemes for ab initio total-energy calculations using a plane-wave basis set. *Phys. Rev. B: Condens. Matter Mater. Phys.* **1996**, *54* (16), 11169−11186. (d) Kresse, G.; Joubert, D. From ultrasoft pseudopotentials to the projector augmented-wave method. *Phys. Rev. B: Condens. Matter Mater. Phys.* **1999**, *59* (3), 1758−1775.

(28) (a) Ong, S. P.; Richards, W. D.; Jain, A.; Hautier, G.; Kocher, M.; Cholia, S.; Gunter, D.; Chevrier, V. L.; Persson, K. A.; Ceder, G. Python Materials Genomics (pymatgen): A robust, open-source python library for materials analysis. *Comput. Mater. Sci.* **2013**, *68*, 314−319. (b) Singh, A. K.; Zhou, L.; Shinde, A.; Suram, S. K.; Montoya, J. H.; Winston, D.; Gregoire, J. M.; Persson, K. A. Electrochemical Stability of Metastable Materials. *Chem. Mater.* **2017**, *29* (23), 10159−10167.

(29) Henkelman, G.; Arnaldsson, A.; Jónsson, H. A fast and robust algorithm for Bader decomposition of charge density. *Comput. Mater. Sci.* **2006**, *36* (3), 354−360.

(30) Grass, M. E.; Karlsson, P. G.; Aksoy, F.; Lundqvist, M.; Wannberg, B.; Mun, B. S.; Hussain, Z.; Liu, Z. New ambient pressure photoemission endstation at Advanced Light Source beamline 9.3.2. *Rev. Sci. Instrum.* **2010**, *81* (5), 053106.

(31) Manceau, A.; Marcus, M. A.; Grangeon, S. Determination of Mn valence states in mixed-valent manganates by XANES spectroscopy. *Am. Mineral.* **2012**, *97*, 816−827.

(32) (a) Westin, G.; Grins, J. Rutile-Type $Mn_{(1-x)}Sb_{(1+x)}O_4$ Phases, $0 \leq x \leq 1/3$, Synthesized by the Sol-Gel Technique. *Acta Chem. Scand.* **1993**, *47*, 1053−1056. (b) Westin, G.; Nygren, M. Sol-Gel Preparation of M-Sb oxides from $Sb(OBu^n)_3$-M-Acetate Precursors with M = Mn, Co, Ni. *J. Mater. Chem.* **1993**, *3* (4), 367−371.

(33) Aykol, M.; Dwaraknath, S. S.; Sun, W.; Persson, K. A. Thermodynamic limit for synthesis of metastable inorganic materials. *Sci. Adv.* **2018**, *4* (4), eaaq0148.

(34) Smith, D. C.; Perseil, E.-A. Sb-rich rutile in the manganese concentrations at St. Marcel-Praborna, Aosta Valley, Italy: petrology and crystal-chemistry. *Mineral. Mag.* **1997**, *61* (408), 655−669.

(35) Biesinger, M. C.; Payne, B. P.; Grosvenor, A. P.; Lau, L. W. M.; Gerson, A. R.; Smart, R. S. Resolving surface chemical states in XPS analysis of first row transition metals, oxides and hydroxides: Cr, Mn, Fe, Co and Ni. *Appl. Surf. Sci.* **2011**, *257* (7), 2717−2730.

(36) (a) Robinson, D. M.; Go, Y. B.; Mui, M.; Gardner, G.; Zhang, Z.; Mastrogiovanni, D.; Garfunkel, E.; Li, J.; Greenblatt, M.; Dismukes, G. C. Photochemical Water Oxidation by Crystalline Polymorphs of Manganese Oxides: Structural Requirements for Catalysis. *J. Am. Chem. Soc.* **2013**, *135* (9), 3494−3501. (b) Smith, P. F.; Deibert, B. J.; Kaushik, S.; Gardner, G.; Hwang, S.; Wang, H.; Al-Sharab, J. F.; Garfunkel, E.; Fabris, L.; Li, J.; Dismukes, G. C. Coordination Geometry and Oxidation State Requirements of Corner-Sharing MnO_6 Octahedra for Water Oxidation Catalysis: An Investigation of Manganite (γ-MnOOH). *ACS Catal.* **2016**, *6* (3), 2089−2099.

(37) Seo, D.-H.; Lee, J.; Urban, A.; Malik, R.; Kang, S.; Ceder, G. The structural and chemical origin of the oxygen redox activity in layered and cation-disordered Li-excess cathode materials. *Nat. Chem.* **2016**, *8*, 692.

(38) Grimaud, A.; Diaz-Morales, O.; Han, B.; Hong, W. T.; Lee, Y.-L.; Giordano, L.; Stoerzinger, K. A.; Koper, M. T. M.; Shao-Horn, Y. Activating lattice oxygen redox reactions in metal oxides to catalyse oxygen evolution. *Nat. Chem.* **2017**, *9*, 457.

DOI: 10.1021/acscatal.8b02689
ACS Catal. 2018, 8, 10938−10948